

PAPER


Statistics of twinning in strained ferroelastics

To cite this article: Xiangdong Ding *et al* 2017 *J. Phys.: Condens. Matter* **29** 394002

View the [article online](#) for updates and enhancements.

Related content


- [Thermal and athermal crackling noise in ferroelastic nanostructures](#)
Z Zhao, X Ding, J Sun *et al.*
- [Avalanches and plastic flow in crystal plasticity: An overview](#)
Stefanos Papanikolaou, Yinan Cui and Nasr Ghoniem
- [Characteristics and controllability of vortices in ferromagnetics, ferroelectrics, and multiferroics](#)
Yue Zheng and W J Chen



Contact Hiden Analytical for further details:
W www.HidenAnalytical.com
E info@hiden.co.uk


CLICK TO VIEW our product catalogue

Instruments for Advanced Science




Gas Analysis

- dynamic measurement of reaction gas streams
- catalysis and thermal analysis
- molecular beam studies
- dissolved species probes
- fermentation, environmental and ecological studies




Surface Science

- UHV-TPD
- SIMS
- end point detection in ion beam etch
- elemental imaging - surface mapping



Plasma Diagnostics

- plasma source characterization
- etch and deposition process reaction kinetic studies
- analysis of neutral and radical species



Vacuum Analysis

- partial pressure measurement and control of process gases
- reactive sputter process control
- vacuum diagnostics
- vacuum coating process monitoring

Statistics of twinning in strained ferroelastics

Xiangdong Ding¹, Oktay Aktas¹, Xiaofei Wang¹, Suzhi Li¹, Ziyuan Zhao¹, Libo Zhang¹, Xiaomei He¹, Turab Lookman², Avadh Saxena² and Jun Sun¹

¹ State Key Laboratory for Mechanical Behavior of Materials, Xi'an Jiao Tong University, Xi'an 710049, People's Republic of China

² Theoretical Division, Los Alamos National Laboratory, Los Alamos, NM 87545, United States of America

E-mail: dingxd@mail.xjtu.edu.cn

Received 1 April 2017, revised 11 June 2017

Accepted for publication 10 July 2017

Published 21 August 2017



Abstract

In this review, we show that the evolution of the microstructure and kinetics of ferroelastic crystals under external shear can be explored by computer simulations of 2D model materials. We find that the nucleation and propagation of twin boundaries in ferroelastics depend sensitively on temperature. In the plastic regime, the evolution of the ferroelastic microstructure under strain deformation maintains a stick-and-slip mechanism in all temperature regimes, whereas the dynamic behavior changes dramatically from power-law statistics at low temperature to a Kohlrausch law at intermediate temperature, and then to a Vogel–Fulcher law at high temperature. In the yield regime, the distribution of jerk energies follows power-law statistics in all temperature regimes for a large range of strain rates. The non-spanning avalanches in the yield regime follow a parabolic temporal profile. The changes of twin pattern and twin boundaries density represent an important step towards domain boundary engineering.

Keywords: avalanche, jerks, domain boundary, strain, statistics, yield, plastic deformation

(Some figures may appear in colour only in the online journal)

1. Introduction

Ferroelastics are materials in which structural domains (or twins) can be ordered or switched by the application of homogeneous stress. They are mechanical analogs of ferroelectrics and ferromagnets where the corresponding degenerate states are spontaneous polarization and magnetization. Pattern formation in ferroelastic materials occurs via twinning and detwinning, which involve simultaneous nucleation, propagation, and annihilation of twin walls.

Ferroelastic microstructures and the resulting domain patterns have been extensively investigated over the past four decades for various reasons. 30% of the Earth's crust and most of the Earth's mantle are formed by ferroelastic minerals, making ferroelastics subject to research in mineralogy and other fields of earth sciences. In geology, the investigation of domain patterns is important to understand the formation of rocks. Ferroelastic microstructures can also affect other

physical properties. In materials, which simultaneously show at least two of the ferroic (ferroelastic, ferroelectric, ferromagnetic) properties (so-called multiferroic), the dynamics of ferroelastic microstructures can affect the switching of functional properties, such as ferroelectric polarization [1]. Moreover, twin boundaries in ferroelastics and their precursors in the paraelastic phase can have functional properties that do not exist in the bulk [2, 3]. These properties include ferroicity [4–8], (super-)conductivity [9–12], piezoelectricity [13], flexoelectricity [14], multiferroicity [14–18], as well as those related to high ionic mobility [11, 19], and 2D electron gas near compositional interfaces [20–23]. For physicists and materials scientists, they are interesting from a fundamental perspective since they allow the study of such properties in one and two dimensions. In addition, the functionality confined to the walls led to the emerging field of domain boundary engineering [2, 4–6]. In this field, twin walls and other functional microstructures in ferroelastics are expected to play an

important role as templates for twin structures [2, 24, 25] in multiferroic devices and those based on the aforementioned properties.

The understanding of the mechanism behind the formation of domain patterns in ferroelastics requires a careful assessment of how many walls are nucleated and annihilated. This dynamic behavior involves fine structures on a nano-meter scale that, collectively, constitute macroscopic switching (see the review in [26]). Therefore, statistical evolution of microstructures is paramount to ultimately monitor and control the domain pattern. The dynamics of ferroelastic domain formation and strain induced de-twinning [27–33] often generate crackling noise [34, 35] due to the displacement discontinuities of propagating domain boundaries. These discontinuities lead to energy dissipation over a wide range of domain sizes and frequencies [34, 36, 37]. Crackling noise is a common phenomenon in nature. For example, the Earth emits intermittent noise in earthquakes. The magnetic analogue of this behavior is Barkhausen noise [38–40], which is released when the magnetization evolves through steps under an applied magnetic field with jerky movements [38–40]. Crackling noise has a close correlation with foreshocks and aftershocks, which are commonly observed in earthquakes [41, 42]. By taking into account the correlations between avalanches and foreshocks, scientists nowadays are investigating avalanches in materials to predict earthquakes and major collapses in, for example, mines [43, 44].

Experimentally, ‘crackling noise’ is generated by rapid changes in microstructures [25, 27–33]. Acoustic emission (AE) is a convenient technique to investigate crackling noise under shear deformation or temperature changes [31]. Other experimental methods include the direct calorimetric observation of heat fluxes, thermal expansion and the non-smooth temperature evolution of the elastic moduli [27, 45]. The energy spectra often consist of a superposition of jerky and smooth components, which depend on the time evolution of twin patterns. Energy jerks often stem from abrupt pinning/de-pinning events, which involves the interaction of twin walls with external defects or jamming of multiple twin walls. Smooth behavior is related to the unpinning movement of twin walls. Typically, AE and heat-flux measurements show jerky energy spectra. The jerk distribution follows power law scaling with an exponent ε that ranges between 1.3 and 2.3 [27, 45–47].

It is not straightforward to obtain a direct link between microstructural changes and energy emissions. Simplified theoretical models (e.g. Bak’s sand-pile model [48–51]), the random field Ising model [37, 52], and renormalization group methods [53], provide a first attempt to understand avalanche behavior and estimate the energy exponents, but they cannot account for the underlying mechanism of evolving microstructures. In addition, twinning/detwinning in piezoelectric and ferroic materials usually involves fine structures on a nano-meter scale that, collectively, constitute macroscopic switching (see the review in [26]). A typical example is the lateral movement of a ferroelectric domain wall. This movement occurs via moving kinks in the wall [54], whose size extends over a few atomic layers. Most macroscopic observations can

only identify the lateral domain wall movement as a time averaged process. The elementary step of the kink movement, on the other hand, is visible only in high time-resolution experiments, such as AE measurements [55]. With the advent of experimental methods such as femtosecond spectroscopy, the investigation of the local jerks has become possible.

Alternatively, molecular dynamics simulations have revealed that most fine structures lead to ‘jerky’ movements and heterogeneities on a sufficiently short time scale [14, 17, 18, 56–58]. Here, the term ‘jerk’ is used as an experimental manifestation in any physical observable of an avalanche. Molecular dynamics simulations have the capability of investigating dynamics microstructures and their corresponding statistical evolution simultaneously, which makes such studies crucial for complete understanding of pattern formation under external fields. In this review, we will show how the microstructural and statistical evolution in ferroelastic crystals under external shear can be explored by computer simulations of a 2D model. These studies are also directly related to the applications aspects of ferroelastic microstructures. Some specific examples, without making the review exhaustive, will be presented.

2. Method

The evolution of twinned structures under shear can be simulated by using simple model assumptions. Such a model for a monatomic structure is shown in figure 1(a) [24, 25, 59, 60]. The interatomic potential consists of nearest neighbor, next-nearest neighbor, and third-nearest neighbor interactions, which are represented by black and red springs, and green lines, respectively in figure 1(a). The selection of these interactions ensures a spontaneous shear of the unit cell. The nearest neighbor springs determine the bulk modulus and the critical temperature of a ferroelastic transition. Here, the transition was chosen to be second order, as inspired by the ferroelastic transition in SrTiO_3 [61]. The next-nearest neighbor springs define the double well potential of the ferroelastic transition, which are related to the shear angle. The ground state of the system corresponds to one of these potential minima and is therefore directly connected to the shear angle (figure 1(b)). The shear angle is chosen so that the ground state is a slightly sheared pseudocubic lattice and the thicknesses of the interfaces or twin walls are of the order of three atomic unit cells. In our simulations, we take this angle to be 4° . This value is typically below that of martensitic materials with shear angles of $\sim 8\text{--}10^\circ$ but slightly larger than for most ferroelastic oxides. The competition between nearest-neighbor and next-nearest neighbor (vertical) springs determines surface relaxations. The third next-nearest-neighbor springs determine the thickness of the twin boundary and the twin density.

The initial condition for the simulations consists of two horizontal twin boundaries (figure 1(c)). The system is allowed to relax completely. Two buffer layers, shown in blue in figure 1(c), transmit the shear to the atoms to allow the dissipation of energy that stems from the applied strain. Under these conditions, a shear strain is applied to the simulated

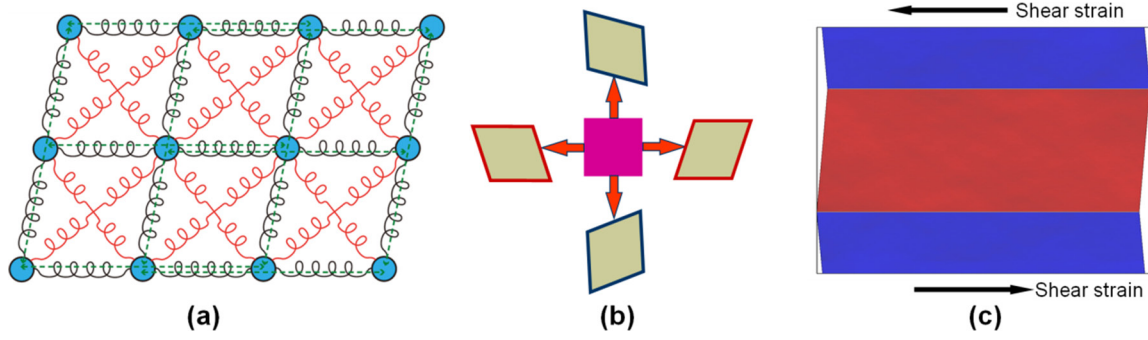


Figure 1. (a) Interatomic potential for a generic ferroelastic model. The model contains nearest-neighbor (black springs), next-nearest-neighbor (red springs), and third-nearest-neighbor (green lines) interactions. The interatomic interactions of this potential are as follows: $V_{\text{hard}}(r) = 20(r - 1)^2$ ($0.8 \leq r \leq 1.2$) and $V_{\text{soft}}(r) = 10(r - 1)^2$ ($0.8 \leq r \leq 1.2$), $V(r) = -10(r - \sqrt{2})^2 + 2000(r - \sqrt{2})^4$ ($1.207 \leq r \leq 1.621$), $V(r) = -(r - 2)^4$ ($1.8 \leq r \leq 2.2$) [25]. (b) Four variant states based on the present potential. (c) The initial sandwich model we used in the simulations. Reprinted with permission from [25]. Copyright 2013, AIP Publishing LLC.

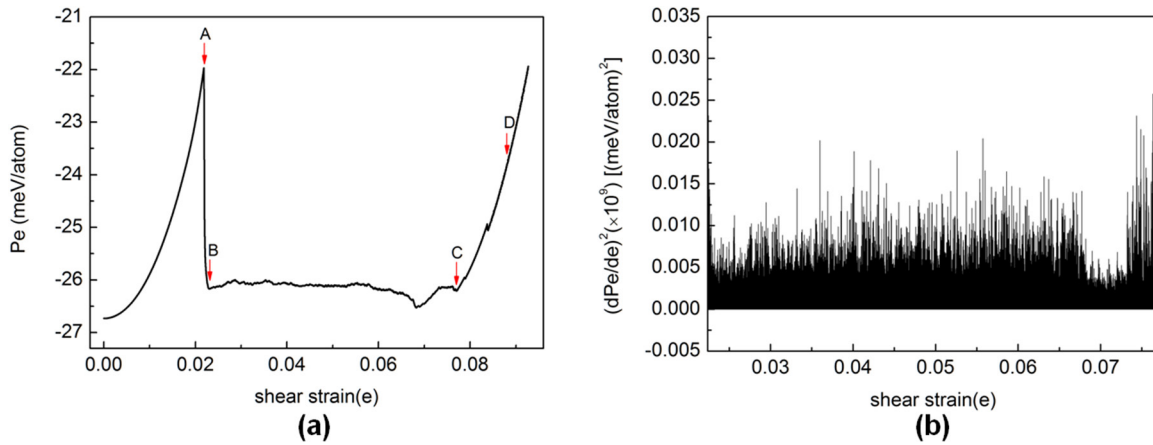


Figure 2. (a) The integrated potential energy (related to the average stress) versus applied strain. Point A is the upper yield point and point B is the lower yield point at which a multi variant twin structure is obtained. On further shearing, the system goes to a single domain state at point C, left a very thin horizontal needle domain. At point D, a perfect single domain state is formed [56]. (b) The energy jerks in the plastic regime between point B and point C. Reprinted figure with permission from [56], Copyright 2013 by the American Physical Society.

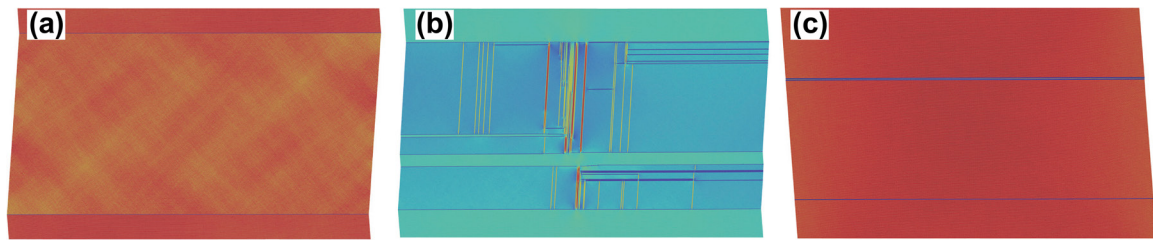


Figure 3. Structure evolution along the potential energy curve in figure 2(a) [59]. (a) Dynamic tweed before point A. (b) Multivariant state at point B. (c) Uniform single domain at point C, except a very thin horizontal needle domain. [59] John Wiley & Sons. Copyright © 2012 WILEY-VCH Verlag GmbH & Co. KGaA, Weinheim.

sample for the investigation of pattern formation and its dynamics.

3. Microstructural evolution and statistics

3.1. Microstructural evolution

The variation of the integrated potential energy with strain is shown in figure 2(a). Elastic energy is pumped to the system (sample) until point A. Points below point A can be described as the elastic regime. The region between A and B corresponds to the yield regime and is characterized by a drastic

drop in the potential energy due to domain nucleation. For points between B and C, the potential energy remains relatively constant since the elastic energy gained due to strain changes the microstructure, i.e. domain pattern. Further strain leads to a single domain state at point D. Strains between B and D correspond to the plastic regime.

In the elastic regime, the shear strain (lower than A) leads to a structural instability. A screen shot of the system in this metastable state is shown in figure 3(a). A cross-hatched pattern is visible between the buffer layers and corresponds to tweed. The tweed structure is dynamic and therefore the pattern changes over short time scale (i.e. flickers). In static, or

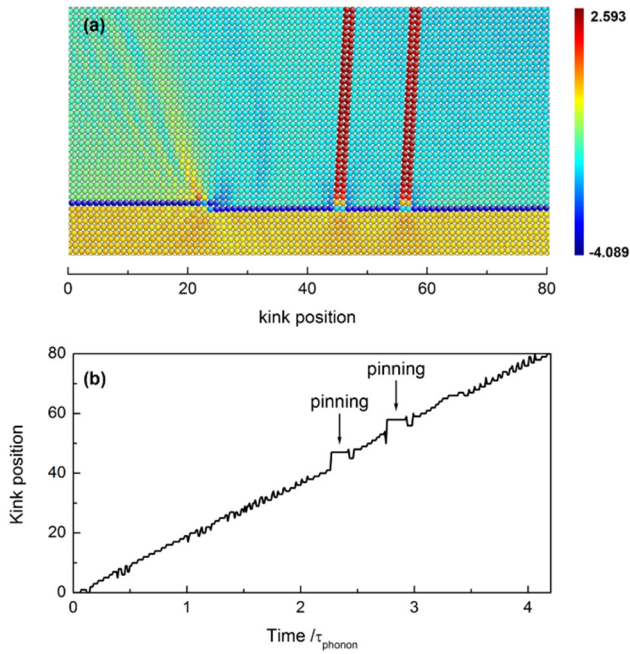


Figure 4. The propagation of a kink through two junctions. (a) Local atomic structure with 80 atoms in domain boundary shows a kink moving towards two junctions. The color scheme represents the local shear angle from the underlying bulk structure ($|\Theta_{\text{vertical}}| - 4^\circ + \Theta_{\text{horizontal}}$), for details see [62]. (b) The corresponding time evolution of the kink position. Two jumps and plateaus indicate attraction, pinning, and retardation, respectively, when the kink reaches the junctions. The speed of the kink is constant when it is far away from the junctions [24]. [24] John Wiley & Sons. Copyright © 2013 WILEY-VCH Verlag GmbH & Co. KGaA, Weinheim.

disorder induced, tweed, which forms due to compositional variations, the direction of tweed is the same as elastically soft directions and parallel to the direction of twin boundaries. This is not the case in dynamic tweed.

With increasing strain (i.e. between points A and B), the dynamic tweed structure transforms into a complex domain pattern. The microstructure at point B obtained at high temperatures, $1.25 T_{\text{VF}}$, where T_{VF} is the Vogel–Fulcher temperature, is shown in figure 3(b). It consists of a multitude of nano-scale domains with a relatively high density of twin intersections. This microstructure is stable. It is noteworthy that the resulting domain pattern is sensitive to changes in temperature. When the system is cooled to a lower temperature ($0.125 T_{\text{VF}}$), the twin pattern in hard materials (i.e. materials with a large bulk modulus k_1) changes, and the density of twin boundaries decreases dramatically. The twin density in soft materials (i.e. materials with a small bulk modulus k_1) is almost unaffected by this temperature decrease.

With strains larger than that at point B, (i.e. in the plastic regime), detwinning occurs through the nucleation of kinks in the twin boundary. The propagating kink overcomes the pinning of horizontal and vertical twin boundaries (the intersections of twins) through a stick-and-slip mechanism (figure 4 [62]). This allows the twin boundary to move towards the surface and detwinning occurs [62]. As the strain reaches the value at point C, the domain pattern decays and only one needle domain remains (figure 3(c)). At point D, the system reaches

a single domain state. The domain pattern at B after the yield point is quite sensitive to changes in the bulk modulus as well as the system size [59]. The size and bulk modulus dependent evolution of the domain pattern is elaborated in section 4.1.

3.2. Distribution of jerks in the plastic regime

The potential energy versus shear strain curves in figure 2(a) are now analyzed in terms of jerk energies. Here, the jerk is defined as the square of the rate of change of potential energy with time, $(dPe/dt)^2$ as shown in figure 2(b). Because the shear strain e increases at a constant rate, one can have the approximation $(dPe/dt)^2 \sim (dPe/de)^2$.

In figure 5, the probability $P(E)$ to find a jerk at energy E is calculated and plotted as a function of jerk energy. The jerk distribution exhibits three major regimes with changes in temperature [56, 62]. At high temperatures ($1.25 T_{\text{VF}}$), the energy distribution of jerks follows Vogel–Fulcher behavior. At intermediate temperatures ($0.125 \times T_{\text{VF}}$), the distribution is described by a generalized Poisson distribution $P(E) \sim E^{-(\gamma-1)} \exp - (E/E_0)^\gamma$ (figure 5(b)) with a stretching exponent n of 0.4 and $\gamma - 1$ being nearly 0. At low temperatures, (figure 5(c)), the distribution changes to power-law behavior $P(E) \sim E^{-(\gamma-1)}$, where the equalities $\gamma - 1 = 2.07$ and $\gamma - 1 = 1.77$ hold for hard and soft materials, respectively, at $1.25 \times 10^{-2} T_{\text{VF}}$. This crossover is in agreement with recent experimental results of a ferroelastic switching process on PbZrO_3 at different temperatures, which shows that the statistics of the squared drop velocity maxima changes from power law at low temperature to exponential law at high temperature due to the thermal fluctuations [63].

The phase diagram of the distribution functions in the plastic regime as a function of temperature is shown in figure 6 (see caption of the figure for details) [64].

3.3. Distribution of jerks in the yield regime

The dynamics of pattern formation in the yield regime is primarily related to a high number of energy jerks related to the nucleation and extension of twin patterns. The majority of these microstructural changes occur in avalanches so that the avalanche energies are scaled by the energy jerks. In the yield regime, these jerks follow power law dynamics [56, 64, 65]. Although the avalanche dynamics of twinning has experimentally been investigated at low strain rates [30, 66, 67], such investigations for high strain rates are not common and very little is known. Two important questions are yet to be answered: does the yield process remain scale invariant for high strain rates. If that is the case, does the energy exponent of the power law distribution of the avalanche formation [35] remain unchanged?

Perez-Reche *et al* attempted to answer these questions for the first time [68] by investigating the effect of thermal driving rates on the avalanche exponents in two alloys, Cu–Zn–Al and Cu–Al–Ni. In Cu–Zn–Al, changes by a factor of 100 in the shear rate lead to a change of 0.3 in the exponents. The typical rate of the length change of a sample in the laboratory is $3 \times 10^{-3} \text{ m s}^{-1}$. The impact of a typical bullet leads to rates in length change of 300 m s^{-1} . This increase, which

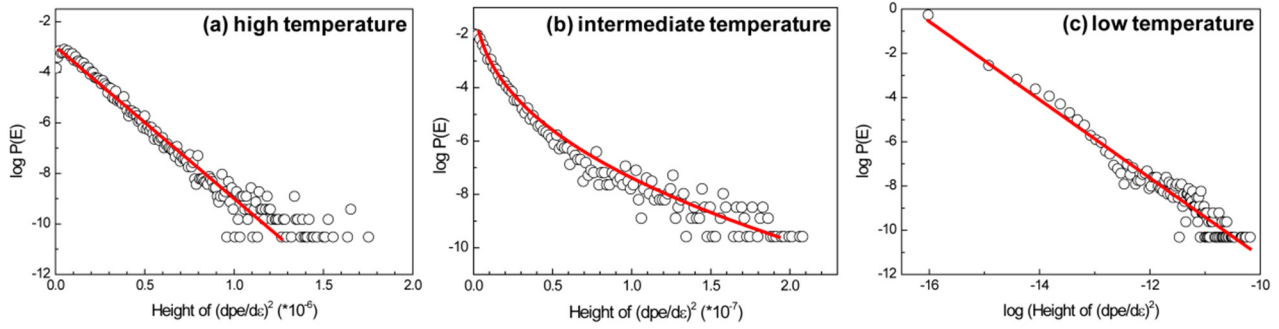


Figure 5. Distribution of jerks from Vogel–Fulcher (a) to stretched exponential (b) to power law (c), in different temperature regimes [56]. Reprinted figure with permission from [56], Copyright 2013 by the American Physical Society.

corresponds to a factor of 10^5 , would lead to a change of 0.6 in the energy exponent. The resolution of a computer simulation experiment is high enough to detect this change. However, no such changes occur according to our model [69], as shown in the following paragraphs.

Figure 7(a) shows a statistical jerk distribution during yield at a strain rate of $5 \times 10^{-6} \tau^{-1}$, which follows power law statistics. All avalanches follow the same statistics with an energy exponent near $\varepsilon = 1.35$. In other words, the energy exponent is the same for all simulations where avalanches could be detected. This value is close to the mean field value [35] for the formation of twin patterns [35]. It was also experimentally observed in martensitic alloy $\text{Cu}_{74.08}\text{--Al}_{23.13}\text{--Be}_{2.79}$ [30] and during the collapse of porous SiO_2 -vycor under compression [70]. Figure 7(b) shows that the energy exponent is independent of the strain rate for relatively high strain rates. On the other hand, Perez-Reche *et al* [68] observed changes in the power law exponent at much lower strain rates. Their observation of the strain rate dependence may be related to the relaxation of external defects and phase mixtures. It may also be due to very slow changes of large twin patterns, which do not exist in fast impact regime considered in our simulations. Such slow relaxations are commonly observed in glasses (so called α -events) but have not been observed during the propagation of individual twin domains [28].

Next, we determine the temporal avalanche profiles normalizing the duration and the peak intensities of three jerk quantities. These quantities are $J(t) = (dU/dt)^2 \sim (dU/de)^2$, the energy drop $J(t) = -(dU/dt) \sim -(dU/de)$, and the shear stress drop $J(t) = -(d\tau_{xy}/dt) \sim -(d\tau_{xy}/de)$, where U is the potential energy, and τ_{xy} is shear stress. The average profiles are then calculated using the superposition of >770 jerks (with more than 5 points in each jerk) [71]. The temporal profiles depend somewhat on the threshold of the jerk spectra (figure 8(a)). Very low thresholds lead to overlaps between small peaks. In this case, small peak profiles do not necessarily correspond to the profiles of single events [35]. Thresholds at higher levels require caution in that the peak duration is underestimated which can lead to an inaccurate temporal profile. To test the proper use of the threshold, four thresholds are used for $(dU/de)^2$. The peak profiles are shown in figures 8(b) and (c). The avalanche profiles of the energy drops $-dU/de$ and the shear stress drops $-d\tau_{xy}/de$ are shown in figures 8(d)–(i), respectively, for which three different thresholds are used. The best fit for all avalanche profiles

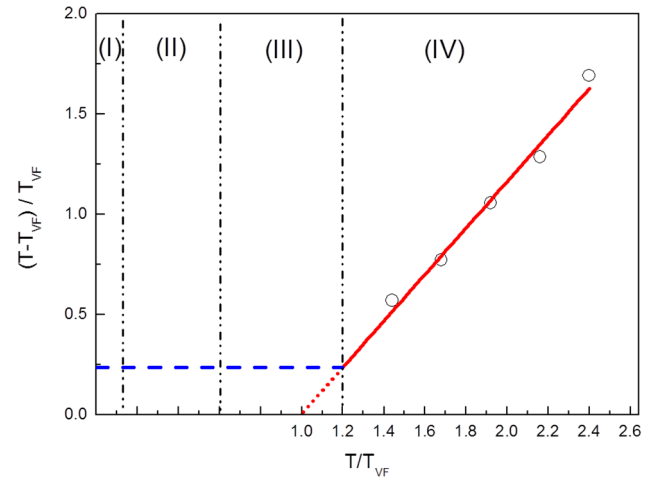


Figure 6. Phase diagram of the distribution functions for the pattern formation as a function of temperature. At very low temperatures, the distribution of the jerky behavior is sparse and probability $P(E)$ to find a ‘jerk’ with an energy E does not follow the power law (regime I). At low temperatures, the process is athermal and follows a power law distribution $P(E) \sim E^{-\varepsilon}$ (regime II). At temperatures above the Vogel–Fulcher temperature T_{VF} , the pattern evolution is thermally activated and $P(E)$ follows Vogel–Fulcher statistics (regime IV). At temperatures between the power-law and Vogel–Fulcher regime, $P(E)$ follows stretched exponential statistics (regime III) [64]. [64] 2013 © TMS 2012. With permission of Springer.

is a universal parabola with $J(t)/J_{\max} = 1 - 4(t/t_{\max} - 0.5)^2$ for immediate threshold (threshold 1 in figure 8). For low thresholds, the quadratic parabola changes to a 4th order parabola and the flattening of the avalanche profile occurs. This behavior is due to severe peak overlap. A similar result is obtained for high thresholds as a result of peak splitting. The broadening of avalanche profiles with changing threshold is consistent with the results obtained in bulk metallic glasses [72]. It is noticeable that the scaling of $(dU/de)^2$ is better defined than the scaling of $-dU/de$ and $-d\tau_{xy}/de$. In all cases, the averaged profiles are always symmetric. Another important result that can be derived from these results is that a quadratic parabola profile is universal for ferroelastic switching avalanches.

A key feature of the simulations presented so far is that they contain no extrinsic defects. It is well understood that defect induced disorder generates avalanches. Our simulations show that, the interaction of twin boundaries generates a high degree of disorder to allow jerks to dominate the noise spectrum.

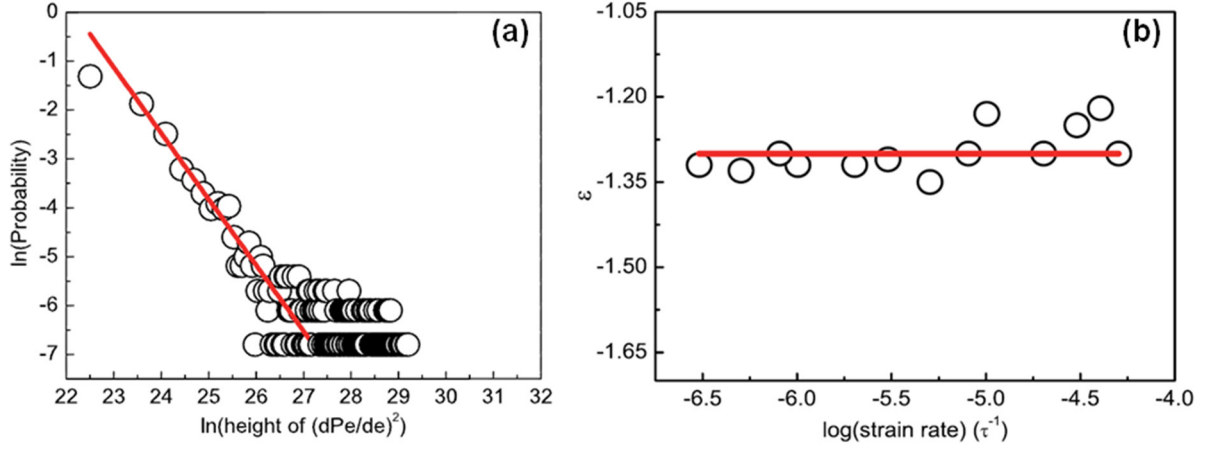


Figure 7. (a) The jerk spectra during the yield event at a strain rate of $5 \times 10^{-6} \tau^{-1}$ show a power law distribution $P(E) \sim E^{-\varepsilon}$ with an energy exponent $\varepsilon = 1.35$. (b) The change of power law exponent ε during the yield event as function of the strain rate, showing that ε is independent of the strain rate [69]. Reprinted with permission from [69]. Copyright 2014, AIP Publishing LLC.

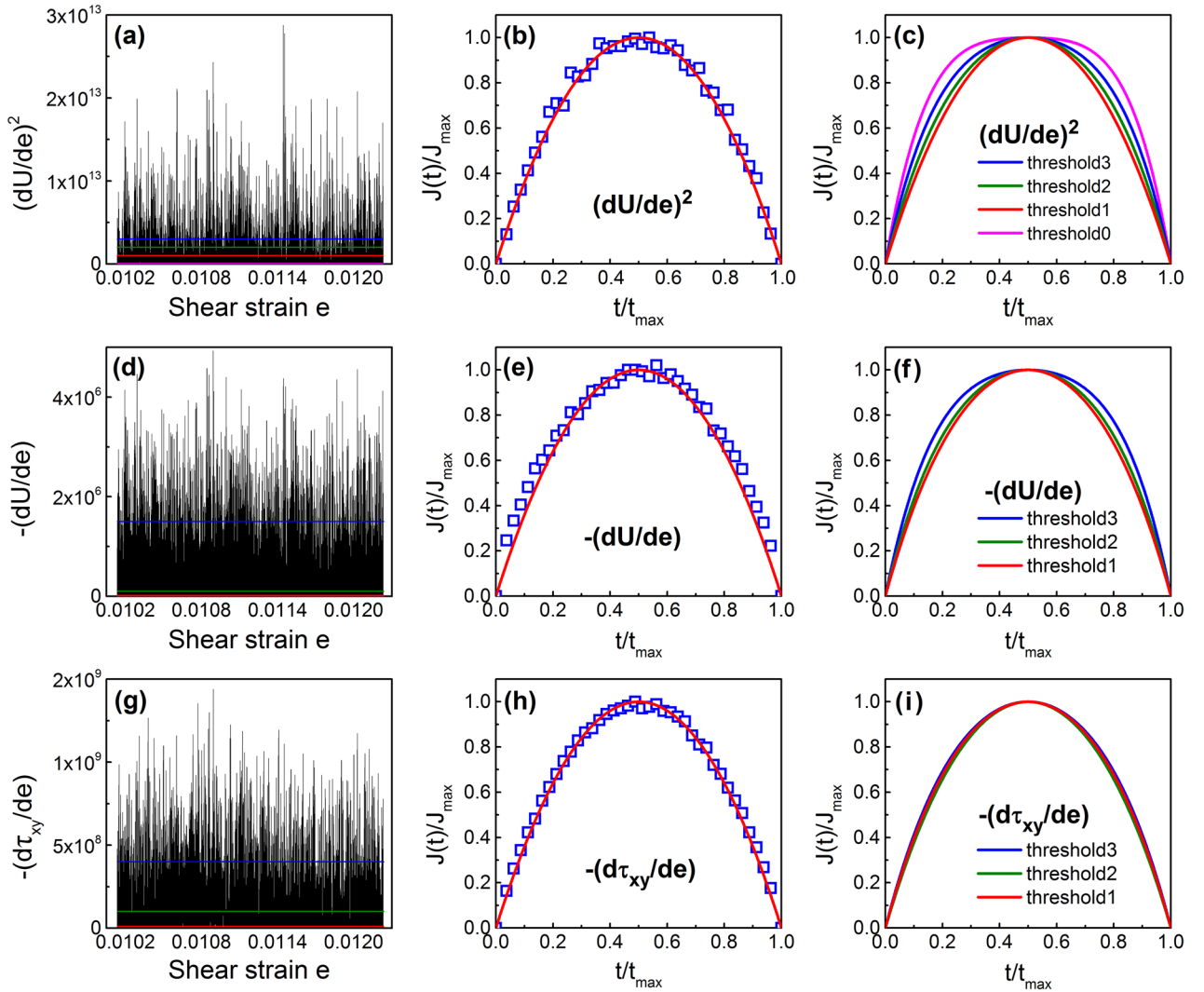


Figure 8. Jerk spectrum of $(dU/de)^2$ (a), $-dU/de$ (d), and $-d\tau_{xy}/de$ (g) at 30 K with various threshold levels. Only peaks above a given threshold were used to calculate the temporal jerk profiles. Temporal jerk profiles of $(dU/de)^2$ (b), $-dU/de$ (e), and $-d\tau_{xy}/de$ (h) show parabolic avalanche profiles: $J(t)/J_{\max} = 1 - 4(t/t_{\max} - 0.5)^2$ (the red line in (b), (c), (e), (f), (h) and (i)). The change of temporal jerk profiles of $(dU/de)^2$ (c), $-dU/de$ (f), and $-d\tau_{xy}/de$ (i) with changing threshold tend towards a 4th order parabola which arises from peak overlap at very low threshold (threshold 0 in (c)) or peak splitting at high threshold (threshold 2 and 3 in (c), (f) and (i)) [71]. Reprinted with permission from [71]. Copyright 2016, AIP Publishing LLC.

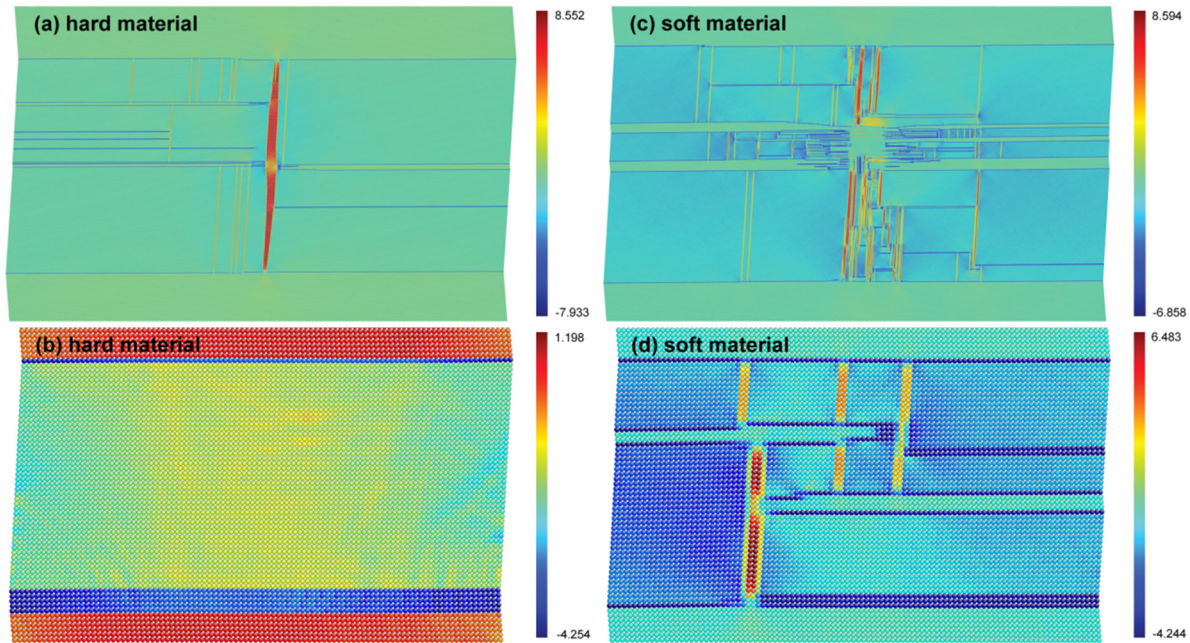


Figure 9. Domain patterns formed after the collapse at the yield stress for a large system with 641600 atoms (top) and a small system (10200 atoms) (bottom). The images on the left represent hard systems. Those on the right are for soft systems (the colors refer to the local shear angles $|\Theta_{\text{vertical}}| - 4^\circ + \Theta_{\text{horizontal}}$) [62]. The network of intersecting twin boundaries forms junctions, which are present even for small systems in a soft material. The network is destroyed as the stable domain invades the unstable region. No vertical walls are seen in small systems of a hard material [59].

It is hence incorrect to postulate that either a defect-free self-organized criticality (SOC) or the presence of disorder from extrinsic defects is paramount to generate avalanches. Many systems with power-law statistics at low temperatures are likely to exhibit a mixture of such jamming and the effect of defects.

4. Some potential applications

The simulations described in the previous section provide insights into the evolution of microstructures and statistics of twinning in ferroelastics. Such understanding is crucial for nano-scale device applications of ferroelastic microstructures. In this section, we will present several findings that are directly related to such applications.

4.1. High junction and twin boundary densities in dynamically driven systems

For applications of twin boundaries and other microstructures in ferroelastics, in particular, those in domain boundary engineering, usually a high density of twin boundaries is required. The most common method to produce high twin wall densities is fast temperature quench from a paraelastic phase into a ferroelastic phase (see the model by Balland James) [73]. By computer simulations, we show here that an alternative method is cold shearing, which is to drive a single domain crystal by shear strain in the low temperature, ferroelastic phase. In this way a large number of long-lived metastable states can be generated kinetically.

In our computer experiment we simulate the shear in a thin film of a ferroelastic material. Both a hard material with

spring constant $k_1 = 20$ and a soft material with $k_1 = 10$ are considered. In both systems, the stress drops by 75% from the upper yield point (A) to the lower yield point (B) [59]. The formation of the twin pattern occurs at an extremely fast time scale (on the order of a few phonon lifetimes), with no creep phenomena near the yield point [74, 75]. The pattern consists of a network of intersecting twin boundaries in both hard and soft systems with a large size (figures 9(a) and (b)). In soft materials there is much larger number of intersections. These intersections, also called junctions, are destroyed when the stable domain invades the unstable region. In small systems of a hard material, the domain patterns within the unstable region are much ‘simpler’ (figure 9(b)). No vertical domain walls exist and the advancement of domain boundaries only occurs by the nucleation and annihilation of kinks in the walls. In addition, with decreasing system size, the number of junctions converges to zero. This behavior significantly differs from soft materials, which still has several junctions (figure 9(d)).

As shown in figure 9, the cold shearing technique leads to complex twin patterns with a high density of twin walls and their intersections, and we call these intersections as junctions. A convenient way to characterize the complexity of the pattern is the number density of junctions. Figure 10 compares the junction densities of hard and soft systems. Hard systems produce fewer junctions with 10^{-4} for large systems, which goes to zero as the system size is decreased. In hard materials, correlations between the twin walls and junctions are strong. This prevents the nucleation of junctions for small system size and leads to parallel twin walls with little interaction between them.

Soft materials generally have higher junction densities (2×10^{-3} for large systems) than those in hard materials. The strong relaxation of these systems allows the formation

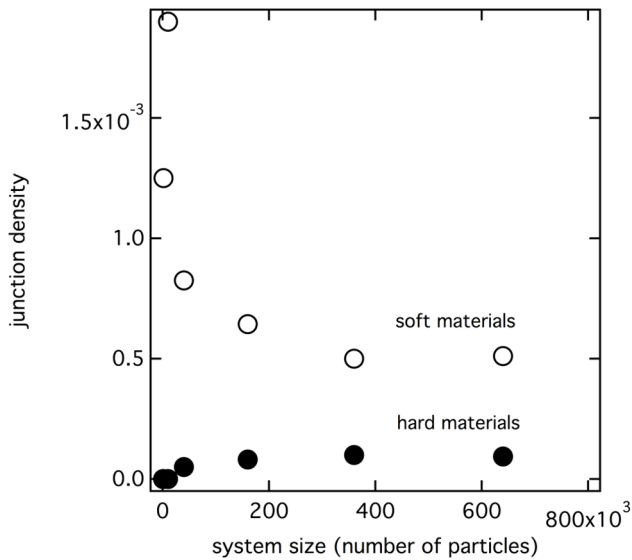


Figure 10. Variation of junction density for hard (full circles) and soft (open circles) thin materials with system size. In soft layers, the strain energy related to junctions is smaller so that intersections between twin walls are common and lead to higher junction densities [59]. A steep increase occurs in the density with decreasing system size. Hard materials have strong correlations between the twin walls and junctions which prevent the nucleation of junctions for small system sizes. This means that twin walls are parallel with little interaction between them. [59] John Wiley & Sons. Copyright © 2012 WILEY-VCH Verlag GmbH & Co. KGaA, Weinheim.

of junctions even in very small samples [76, 77]. Therefore, soft materials are better suited for applications in domain boundary engineering where a high density of twin wall and junction densities are required. So far, the junction density of a ferroelastic material has not been reported. Based on the results presented, we estimate the twin density in large, soft materials (figure 9(c)) to be 5% of the total ‘volume’. This value is in reasonable agreement with values observed in WO_3 and LaAlO_3 (0.3% found in a pattern with parallel walls) [78, 79], orthoclase (2%) [79], and Co-doped YBCO (2.8%) [80]. According to the Kittel formula for ultrathin films [5], concentrations that are much larger than 4% of the domain wall material can be expected. In TbMnO_3 twin domains as small as 5 nm have been reported [81]. This suggests that the number of atoms inside twin walls can be close to 50%. In ferroelectric superlattices such small domain sizes were also reported and walls were found to be chiral and form vortices [82]. This has significant implications for device applications since a large density of twin walls and their functionality (i.e. chirality) coexist. Applications based on functional twin walls, such as memory devices, elastic dampers, and heat regulators can be anticipated in the future.

4.2. Strain-controlled thermal conductivity and thermal memory

Here we will show that the nucleation and growth of twin boundaries reduces thermal conductivity if the heat flow is perpendicular to the twin walls, which act as phonon barriers. By using strain to manipulate the twin pattern, the thermal conductivity can be reversibly controlled [83].

A shear strain with strain tensor as $[0, 0, e_{xy}]^T$ is applied to a sample. The resulting stress–strain curve under loading and unloading is depicted in figure 11(a). Under loading (black curve) the sample yields when the strain e_{xy} reaches $\sim 0.6\%$. During unloading (red curve), strain decreases from $e_{xy} = 1.6\%$ to zero (red curve). The variation of thermal conductivity during the loading and unloading is shown in figure 11(b). In the elastic regime, the change in the magnitude of thermal conductivity κ is negligible (~ 140 to 150 r.u.) under stress. During loading into the plastic regime, κ undergoes an abrupt drop by almost one half of its initial value, i.e. from ~ 150 to 90 r.u. This value remains invariant under further stress. When the system is unloaded, the thermal conductivity reaches back to its initial value and the loading and unloading cycle thus shows hysteretic behavior. These results show that the mechanical control of the microstructure enables the control of the thermal conductivity. Therefore, this approach is an alternative to control the intrinsic properties of the single domain state. By controlling the microstructure, one can generate two logic states, one with high heat conduction (e.g. points (c) and (f) in figure 11(b)) and the other with low heat conduction (e.g. points (d) and (e) in figure 11(b)). Systematic generation of two such logic states may find applications in thermal information storage and thermal switching [84, 85].

In order to determine the mechanism of the hysteretic behavior of thermal conductivity under a loading and unloading cycle, the evolution of twin patterns for several strains are examined. The strains are marked as (c)–(f) in figure 11(b)) and the corresponding twin patterns are shown in figures 11(c)–(f). Under plastic deformation with shear strain, new horizontal (HTBs) and vertical twin (VTBs) boundaries are nucleated. The nucleation of VTBs starts from one horizontal twin boundary (HTB) and ends in another horizontal twin boundary. The nucleated VTBs and HTBs superimpose and finally evolve into a complicated twin pattern, which significantly reduces the thermal conductivity compared to the single domain state. Moreover, the structure of the twin pattern is quite stable and the twinning morphology shows negligible changes when a temperature gradient is applied in non-equilibrium molecular dynamics (NEMD) calculations. Upon unloading, horizontal twins are preserved, which permanently deforms the sample. On the other hand, the vertical twins are unstable and gradually vanish as the load is removed, which leads to an increase in κ .

These results show that the reduction of thermal conductivity stems from the nucleation of vertical twin walls with an orientation perpendicular to the heat flow. To further elucidate the exact role of VTBs and HTBs in thermal conductivity, the variations of both VTB density (ρ_{VTB}) and HTB density (ρ_{HTB}) in the loading/unloading cycle are determined. Here, twin wall densities in our 2D system are defined as the ratio of the twin boundary area to the total area of the system, given in units of a^{-1} . Figure 11(g), where the VTB density is plotted against shear strain, show along with figure 11(b) a direct correlation between the nucleation and annihilation of vertical twins and changes in the thermal conductivity. The nucleation of VTBs reduces thermal transport. As the strain reaches the upper yield point ($e_{xy} = 0.8\%$), VTBs begin to nucleate, which results in an abrupt drop in the thermal conductivity.

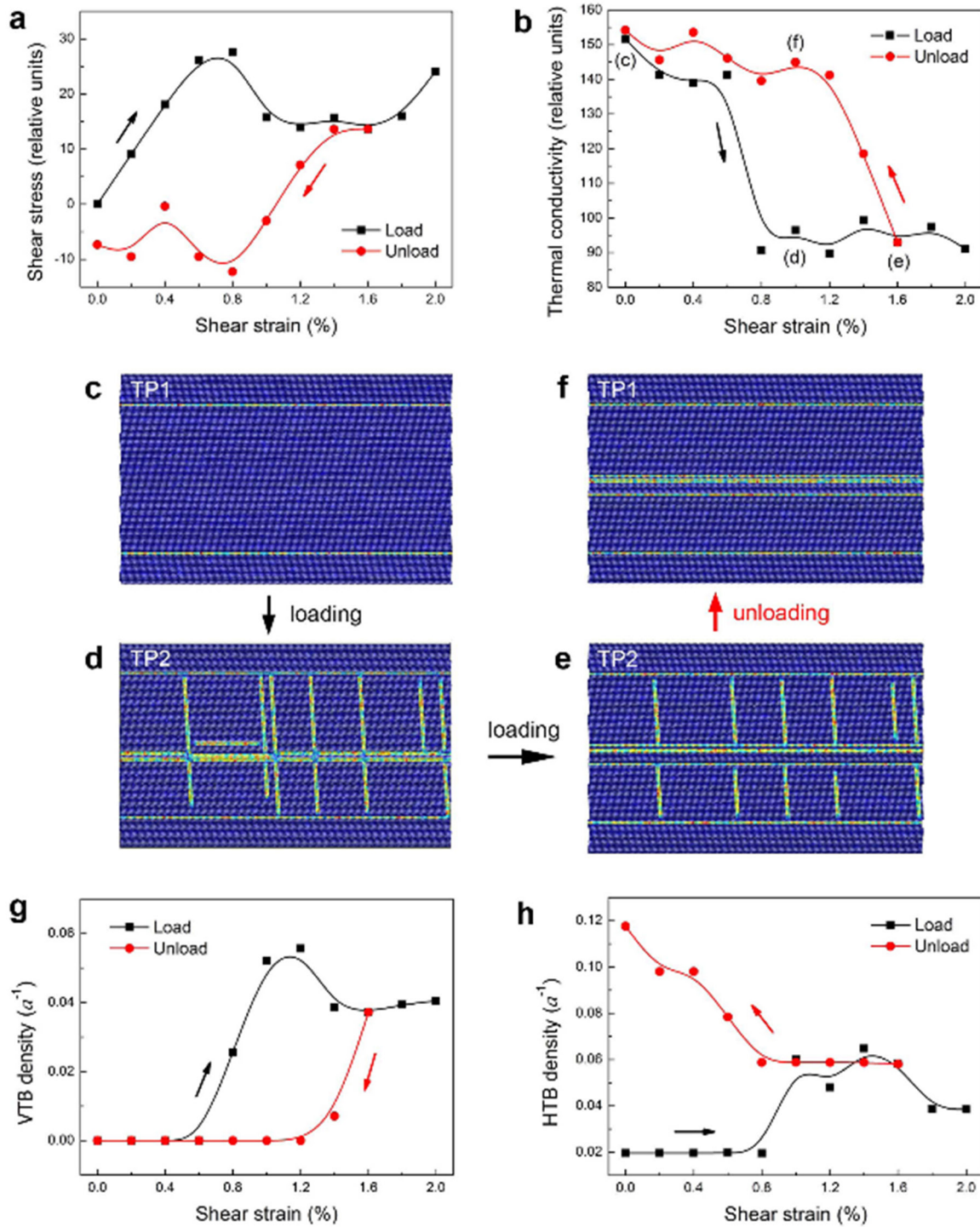


Figure 11. Strain-control of thermal conductivity in twinned films. (a) Stress-strain curve in a simple shear loop. (b) Variation of thermal conductivity with shear strain. (c)–(e) Representative atomic images corresponding to the different strain-scenarios marked in (b). Twin pattern 1 (TP1) in absence of vertical twin boundaries (VTBs) has a lower thermal conductivity than twin pattern 2 (TP2) with VTBs. Density of (g) VTBs and (h) HTBs as a function of shear strain, in units of \AA^{-1} . Atoms are colored by centro-symmetry parameters [87]. Reprinted by permission from Macmillan Publishers Ltd: [Scientific Reports] [87], Copyright 2014.

The magnitude of ρ_{VTB} reaches the maximum value at lower yield point ($\epsilon_{xy} = 1.0\%$) and remains relatively constant under further shearing ($1.0\% - 2.0\%$), similar to the stress evolution of the thermal conductivity which also remains unchanged in the same strain range. Unlike VTBs, the formation of horizontal

twins does not influence the heat transport and the thermal conductivity is independent of the density of HTBs (figure 11(h)).

Our results agree well with the experimental observation that the existence of twins in ferroelastic $\text{Gd}_2(\text{MoO}_4)_3$ reduces thermal conductivity largely in comparison with a monodomain

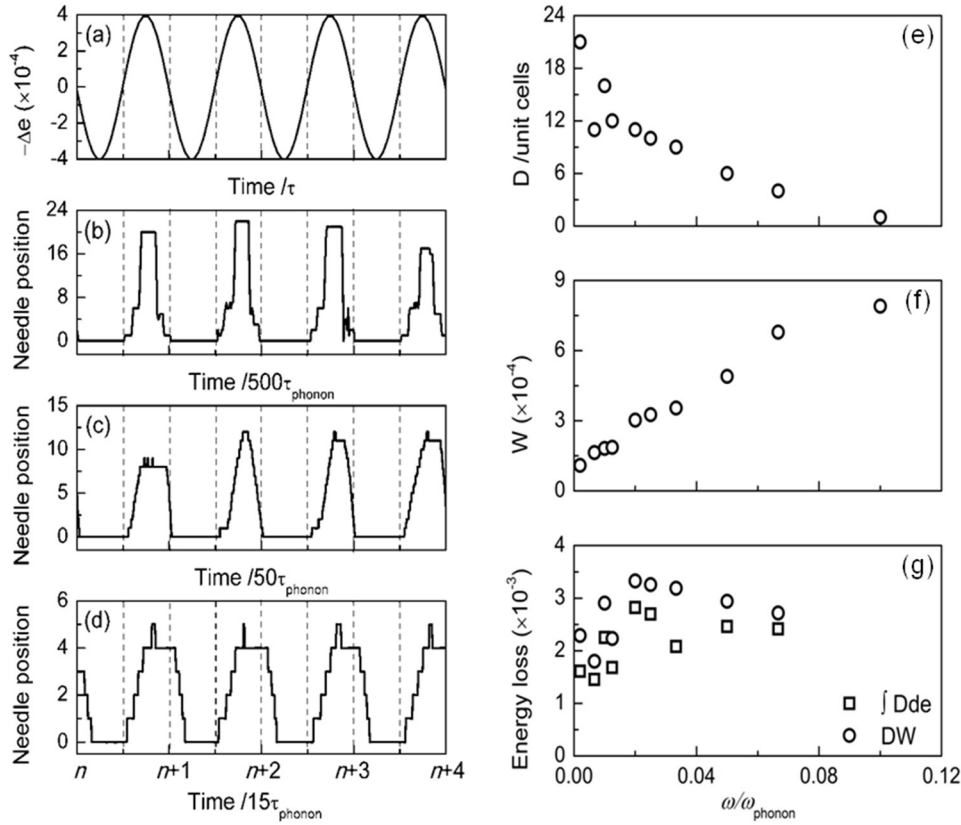


Figure 12. (a)–(d) Position of the needle tip compared with the driving strain oscillation ($\Delta e = A \sin(\omega t)$). τ is the time period of input sine-wave and τ_{phonon} is the time period of phonons. Note the increasing width of the profile when the frequency is increased. The onset of the domain retraction is retarded with respect to the reflection points of the driving force while the progression of the needle starts later than the reversed driving strain (Δe). The profiles are non-symmetric with slow retraction and faster progression. Frequency dependence of (e) the gap, D , between the needle tip and the orthogonal twin boundary, (f) the width of the strain hysteresis, W , and (g) the product DW (circle symbols) (also evaluated as an integral over the strain hysteresis (square symbols)). This figure shows that although the gap (D) and the width of the strain hysteresis (W) is a function of frequency, the energy loss by the pinning/de-pinning of needles is (almost) independent of frequency [24]. [24] John Wiley & Sons. Copyright © 2013 WILEY-VCH Verlag GmbH & Co. KGaA, Weinheim.

sample [86]. These results are also in line with phonon participation ratio p_λ , details of which can be found in [87].

4.3. Mechanical loss in multiferroic materials at high frequencies: friction and the evolution of ferroelastic microstructures

The above results show that we can control the microstructure of materials and obtain novel properties. In this section, we show that microstructural changes under cyclic load may also bring about unwanted phenomena, such as energy loss.

The development of multiferroic device materials encounters a fundamental limitation for frequencies beyond 50 MHz. Detectors, memory chips and converters between electric and magnetic signals operating at such high frequencies are potential devices based on multiferroics. These applications require defect free device materials because any extrinsic defect relaxation will be slower than the operating frequency and will hence absorb the external signal [88–90]. A trivial idea to solve this problem is to use ‘clean’ multiferroic materials (i.e. nearly defect free) so that defects are too few to influence the switching of electric and magnetic dipoles. Nevertheless, as shown in this section, this solution does not work in most materials where coupling to ferroelasticity is

strong. It is already known based on experimental observations that domain boundary motion in ferroelastic materials involves high losses and is highly dissipative (e.g. in relaxor materials) [12, 91]. However, the origin of these energy losses was unclear. In this section we demonstrate that two mechanisms, namely, the propagation of needle domains and the movements of wall kinks, dominate the loss effects.

The dynamic behavior of a single needle domain under oscillating strain is as follows. In the first five cycle the needle domain consolidates the microstructure. Afterwards, it disconnects from the horizontal twin boundary during parts of the driving cycle, which is typical for metastable domain patterns without further strain. We set the external strain e_0 at the de-pinning point where the needle just detaches itself from the horizontal twin boundary. Increasing the strain by Δe then stabilizes the domain pattern. If the strain is reduced during the negative half period of the sine wave, however, the needle domain is destabilized, which causes the junction between the needle domain and the horizontal twin boundary to rupture. Then, it can freely retract and progress when the strain increases. A representative sequence of such oscillations is shown in figure 12. These experiments were repeated over several cycles and over a large frequency range between $\omega = \omega_{\text{phonon}}/10$ and $\omega = \omega_{\text{phonon}}/500$ (where ω_{phonon} is the

phonon frequency). The results demonstrate that there is a large phase angle between the exciting wave and the tip position and this angle varies with frequency. This was experimentally observed with resonant ultrasound spectroscopy measurements but was not explained before [92, 93].

Figure 12(e) shows that, D = maximum distance between the needle tip and the pinning horizontal twin wall, or the amplitude of the ‘free’ movement of the needle, decreases as the frequency is increased, which is opposite to the frequency dependence of the width of the ferroelastic hysteresis (W) (figure 12(f)). The width W is well defined with small thermal fluctuations at high frequencies. This is not the case for the amplitude (D) at low frequencies where it shows fluctuations as high as 30% when the shear excitation is continued over several periods (figures 12(b) and (e)). The amplitude of the fluctuations decreases with increasing frequency (figures 12(c) and (d)). This is because at higher frequencies the time scale for the propagation is determined by the time scale of the exciting shear wave and not by the thermal fluctuations during the needle propagation. The integrated hysteresis ($\int Dde$) and the product DW , which can also be used to estimate the integrated hysteresis, are plotted in figure 12(g). Both display large fluctuations at low frequencies. In addition they show that the energy loss is nearly independent of frequency.

Another loss of energy dissipation in ferroelastics under oscillating strain is the propagation of kinks (see [24] for details). The speed of the movement of the kink is almost constant. The kink accelerates only if the direction of movement is inverted and this acceleration is frequency dependent. The constant speed of the kink (in a defect free system) results from phonon scattering. The scattering of phonons leads to localized dynamic lattice distortions following the moving kink. This effect resembles propagating acoustic phonons which transfer friction loss into the bulk. This phonon drag prevents the acceleration of the kink movement. If the driving strain is larger than that required for the movement of the kink, phonons absorb the excess energy and no visible effect on the kink movement can be seen [24, 94].

5. Summary

By developing a 2D toy model, we systematically investigated the evolution of microstructure and statistics of twinning in ferroelastics under external shear. In the plastic regime, a temperature phase diagram that shows different regimes of jerk behavior as a function of temperature is established. In the yield regime, the power law distributions of jerk energy and parabolic temporal profiles are confirmed in all thermal regimes and a large range of strain rate. Some potential applications of functional domain boundaries are also explored.

Future challenges include the behavior in the presence of defects as well as the exploration of functional domain boundaries in ferroelastics. There is a need to develop a model to account for the evolution of ferroelectric domain boundaries in ferroelastics and predict the related novel properties related to ferroelastic domain boundaries.

Finally, simulations are very appropriate for the analysis of energy loss and damping effects in ferroelastic samples and the coupling with other ferroic properties. An example is coupling with magnetism and the formation of complex ferroelectric patterns [95]. Damping can in such cases be determined either directly from the energy loss spectrum or via the Kramers–Kronig (KK) relationship from the frequency dependence of the real part of the elastic moduli. A novel approach is to compare these two data sets and determine whether the loss-response is linear, in which case the KK data and the direct loss data coincide. If, on the other hand, the response is highly non-linear, the agreement is poor and warrants further in-depth analysis [96].

Acknowledgments

We appreciate the support of the Natural Science Foundation of China (51320105014, 51621063, 51231008) and 111 project (B06025). This work was also supported in part by the Engineering and Physical Sciences Research Council (EP/K009702/1) and the Leverhulme Foundation (RPG-2012-564) and the US Department of Energy.

References

- [1] Gao P *et al* 2014 *Nat. Commun.* **5** 3801
- [2] Salje E 2012 *Annu. Rev. Mater. Res.* **42** 265–83
- [3] Salje E, Ding X and Aktas O 2014 *Phys. Status Solidi b* **251** 2061–6
- [4] Salje E and Zhang H 2009 *Phase Transit.* **82** 452–69
- [5] Salje E K H 2010 *ChemPhysChem* **11** 940–50
- [6] Van Aert S, Turner S, Delville R, Schryvers D, Tendeloo G V and Salje E K H 2012 *Adv. Mater.* **24** 523–7
- [7] Kalisky B, Kirtley J R, Analytis J G, Chu J H, Fisher I R and Moler K A 2011 *Phys. Rev. B* **83** 064511
- [8] Ivry Y, Chu D, Scott J F, Salje E K H and Durkan C 2011 *Nano Lett.* **11** 4619–25
- [9] Aird A and Salje E K H 1998 *J. Phys.: Condens. Matter* **10** L377–80
- [10] Kim Y, Alexe M and Salje E K H 2010 *Appl. Phys. Lett.* **96** 032904
- [11] Seidel J *et al* 2010 *Phys. Rev. Lett.* **105** 197603
- [12] Catalan G, Seidel J, Ramesh R and Scott J 2012 *Rev. Mod. Phys.* **84** 119–56
- [13] Salje E, Aktas O, Carpenter M, Laguta V and Scott J 2013 *Phys. Rev. Lett.* **111** 247603
- [14] Salje E, Li S, Stengel M, Gumbsch P and Ding X 2016 *Phys. Rev. B* **94** 024114
- [15] Lubk A, Gemming S and Spaldin N A 2009 *Phys. Rev. B* **80** 104110
- [16] Lottermoser T and Fiebig M 2004 *Phys. Rev. B* **70** 220407
- [17] Zhao Z, Ding X and Salje E 2014 *Appl. Phys. Lett.* **105** 112906
- [18] Salje E, Li S, Zhao Z, Gumbsch P and Ding X 2015 *Appl. Phys. Lett.* **106** 212907
- [19] Calleja M, Dove M T and Salje E K H 2003 *J. Phys.: Condens. Matter* **15** 2301–8
- [20] Ohtomo A and Hwang H Y 2004 *Nature* **427** 423–6
- [21] Pauli S A, Leake S J, Delley B, Björck M, Schneider C W, Schlepütz C M, Martocchia D, Paetel S, Mannhart J and Willmott P R 2011 *Phys. Rev. Lett.* **106** 036101

- [22] Huijben M, Rijnders G, Blank D H A, Bals S, Van Aert S, Verbeeck J, Van Tendeloo G, Brinkman A and Hilgenkamp H 2006 *Nat. Mater.* **5** 556–60
- [23] Herranz G *et al* 2007 *Phys. Rev. Lett.* **98** 216803
- [24] Zhao Z, Ding X, Lookman T, Sun J and Salje E 2013 *Adv. Mater.* **25** 3244–8
- [25] Salje E, Ding X and Zhao Z 2013 *Appl. Phys. Lett.* **102** 152909
- [26] Shaw T, Trolrier-McKinstry S and McIntyre P 2000 *Annu. Rev. Mater. Sci.* **30** 263–98
- [27] Gallardo M C, Manchado J, Romero F J, del Cerro J, Salje E K H, Planes A, Vives E, Romero R and Stipcich M 2010 *Phys. Rev. B* **81** 174102
- [28] Harrison R J and Salje E K H 2010 *Appl. Phys. Lett.* **97** 021907
- [29] Salje E K H, Zhang H, Idrissi H, Schryvers D, Carpenter M A, Moya X and Planes A 2009 *Phys. Rev. B* **80** 134114
- [30] Salje E K H, Koppensteiner J, Reinecker M, Schranz W and Planes A 2009 *Appl. Phys. Lett.* **95** 231908
- [31] Carrillo L, Mansa L, Ortín J, Planes A and Vives E 1998 *Phys. Rev. Lett.* **81** 1889–92
- [32] Ahluwalia R and Ananthakrishna G 2001 *Phys. Rev. Lett.* **86** 4076–9
- [33] Vives E, Ortín J, Mansa L, Ràfols I, Pérez-Magrané R and Planes A 1994 *Phys. Rev. Lett.* **72** 1694–7
- [34] Sethna J P, Dahmen K A and Myers C R 2001 *Nature* **410** 242–50
- [35] Salje E K H and Dahmen K A 2014 *Annu. Rev. Condens. Matter Phys.* **5** 233–54
- [36] Pérez-Reche F J, Vives E, Mansa L and Planes A 2001 *Phys. Rev. Lett.* **87** 195701
- [37] Paczuski M, Maslov S and Bak P 1996 *Phys. Rev. E* **53** 414–43
- [38] Baró J, Dixon S, Edwards R S, Fan Y, Keeble D S, Mansa L, Planes A and Vives E 2013 *Phys. Rev. B* **88** 174108
- [39] Spasojević D, Bukvić S, Milošević S and Stanley H E 1996 *Phys. Rev. E* **54** 2531–46
- [40] Zapperi S, Cizeau P, Durin G and Stanley H E 1998 *Phys. Rev. B* **58** 6353–66
- [41] Hergarten S and Neugebauer H J 2002 *Phys. Rev. Lett.* **88** 238501
- [42] Bowman D D and King G C P 2001 *Geophys. Res. Lett.* **28** 4039–42
- [43] Friedman N, Jennings A T, Tsekenis G, Kim J, Tao M, Uhl J T, Greer J R and Dahmen K A 2012 *Phys. Rev. Lett.* **109** 095507
- [44] Salje E K H, Soto-Parra D E, Planes A, Vives E, Reinecker M and Schranz W 2011 *Phil. Mag. Lett.* **91** 554–60
- [45] Romero F, Manchado J, Martín-Olalla J M, Gallardo M and Salje E 2011 *Appl. Phys. Lett.* **99** 011906
- [46] Castillo-Villa P, Baró J, Planes A, Salje E K H, Sellappan P, Kriven W M and Vives E 2013 *J. Phys.: Condens. Matter* **25** 292202
- [47] Papanikolaou S, Bohn F, Sommer R L, Durin G, Zapperi S and Sethna J 2011 *Nat. Phys.* **7** 316–20
- [48] Frette V, Christensen K, Malthe-Sørenssen A, Feder J, Jossang T and Meakin P 1996 *Nature* **379** 49–52
- [49] Bak P, Tang C and Wiesenfeld K 1987 *Phys. Rev. Lett.* **59** 381–4
- [50] Bak P, Tang C and Wiesenfeld K 1988 *Phys. Rev. A* **38** 364–74
- [51] Bak P and Sneppen K 1993 *Phys. Rev. Lett.* **71** 4083–6
- [52] White R A and Dahmen K A 2003 *Phys. Rev. Lett.* **91** 085702
- [53] Dahmen K and Sethna J P 1996 *Phys. Rev. B* **53** 14872–905
- [54] Salje E, Wang X, Ding X and Sun J 2014 *Phys. Rev. B* **90** 064103
- [55] Dul'kin E, Salje E, Aktas O, Whatmore R and Roth M 2014 *Appl. Phys. Lett.* **105** 212901
- [56] Ding X, Lookman T, Zhao Z, Saxena A, Sun J and Salje E 2013 *Phys. Rev. B* **87** 094109
- [57] Dahmen K, Ben-Zion Y and Uhl J 2009 *Phys. Rev. Lett.* **102** 175501
- [58] Perkovic O, Dahmen K and Sethna J 1999 *Phys. Rev. B* **59** 6106–19
- [59] Ding X, Zhao Z, Lookman T, Saxena A and Salje E K H 2012 *Adv. Mater.* **24** 5385–9
- [60] Salje E, Ding X, Zhao Z and Lookman T 2012 *Appl. Phys. Lett.* **100** 222905
- [61] Salje E, Gallardo M, Jimenez J, Romero F and del Cerro J 1998 *J. Phys.: Condens. Matter* **10** 5535–43
- [62] Salje E, Ding X, Zhao Z, Lookman T and Saxena A 2011 *Phys. Rev. B* **83** 104109
- [63] Puchberger S, Soprunyuk V, Schranz W, Troster A, Roleder K, Majchrowski A, Carpenter M A and Salje E 2017 *APL Mater.* **5** 046102
- [64] Ding X, Lookman T, Salje E and Saxena A 2013 *JOM* **65** 401–7
- [65] Zhao Z, Ding X, Sun J and Salje E 2014 *J. Phys.: Condens. Matter* **26** 142201
- [66] Niemann R, Baro J, Heczko O, Schultz L, Fahler S, Vives E, Manosa L and Planes A 2012 *Phys. Rev. B* **86** 214101
- [67] Bonnot E, Vives E, Manosa L, Planes A and Romero R 2008 *Phys. Rev. B* **78** 094104
- [68] Perez-Reche E, Tadic B, Manosa L, Planes A and Vives E 2004 *Phys. Rev. Lett.* **93** 195701
- [69] Zhang L, Salje E, Ding X and Sun J 2014 *Appl. Phys. Lett.* **104** 162906
- [70] Baro J, Corral A, Illa X, Planes A, Salje E, Schranz W, Soto-Parra D and Vives E 2013 *Phys. Rev. Lett.* **110** 088702
- [71] He X, Ding X, Sun J and Salje E 2016 *Appl. Phys. Lett.* **108** 072904
- [72] Antonaglia J, Wright W, Gu X, Byer R, Hufnagel T and Dahmen K 2014 *Phys. Rev. Lett.* **112** 155501
- [73] Ball J M and James R D 1987 *Arch. Ration. Mech. Anal.* **100** 13–52
- [74] Kleemann W 2007 *Annu. Rev. Mater. Res.* **37** 415–48
- [75] Bajpai A, Borisov P, Gorantla S, Klingeler R, Thomas J, Gemming T, Kleemann W and Büchener B 2010 *EPL* **91** 17006
- [76] Zhu Y, Liao X and Wu X 2012 *Prog. Mater. Sci.* **57** 1–62
- [77] Zhu L, Ruan H, Li X, Dao M, Gao H and Lu J 2011 *Acta Mater.* **59** 5544–57
- [78] Chrosch J and Salje E 1999 *J. Appl. Phys.* **85** 722–7
- [79] Hayward S, Chrosch J, Salje E and Carpenter M 1996 *Eur. J. Miner.* **8** 1301–10
- [80] Schmah W *et al* 1989 *Phil. Mag. Lett.* **60** 241–8
- [81] Daumont C, Mannix D, Venkatesan S, Rubi D, Catalan G, Kooi B, de Hosson J and Noheda B 2009 *J. Phys.: Condens. Matter* **21** 182001
- [82] Yadav A *et al* 2016 *Nature* **530** 198–201
- [83] Ding X and Salje E 2015 *AIP Adv.* **5** 053604
- [84] Xie R, Bui C, Varghese B, Zhang Q, Sow C, Li B and Thong J 2011 *Adv. Funct. Mater.* **21** 1602–7
- [85] Wang L and Li B 2008 *Phys. Rev. Lett.* **101** 267203
- [86] Mielcarek S, Mróz B, Tylczyński Z, Piskunowicz P, Trybuła Z and Bromberek M 2001 *Physica B* **299** 83–7
- [87] Li S, Ding X, Ren J, Moya X, Li J, Sun J and Salje E 2014 *Sci. Rep.* **4** 6375
- [88] Correa M, Kumar A, Priya S, Katiyar R and Scott J 2011 *Phys. Rev. B* **83** 014302
- [89] Eerenstein W, Mathur N and Scott J 2006 *Nature* **442** 759–65
- [90] Scott J 2007 *Nat. Mater.* **6** 256–7
- [91] Carpenter M, Bryson J, Catalan G, Zhang S and Donnelly N 2012 *J. Phys.: Condens. Matter* **24** 045902
- [92] Stepkova V, Marton P and Hlinka J 2012 *J. Phys.: Condens. Matter* **24** 212201
- [93] Salje E and Carpenter M 2011 *Appl. Phys. Lett.* **99** 051907
- [94] Salje E, Zhao Z, Ding X and Sun J 2013 *Am. Miner.* **98** 1449–58
- [95] Fontcuberta J, Skumryev V, Laukhin V, Granados X and Salje E 2015 *Sci. Rep.* **5** 13784
- [96] Safarik D, Salje E and Lashley J 2010 *Appl. Phys. Lett.* **97** 111907